Highly Scalable, Atomically Thin WSe_2 Grown *via* Metal–Organic Chemical Vapor Deposition

Sarah M. Eichfeld,[†,‡] Lorraine Hossain,[†,‡] Yu-Chuan Lin,[†,‡] Aleksander F. Piasecki,[†,‡] Benjamin Kupp,[†,‡] A. Glen Birdwell,[∥] Robert A. Burke,[∥] Ning Lu,[§] Xin Peng,[§] Jie Li,[⊥] Angelica Azcatl,[§] Stephen McDonnell,[§] Robert M. Wallace,[§] Moon J. Kim,[§] Theresa S. Mayer,[‡,⊥] Joan M. Redwing,[†,‡] and Joshua A. Robinson*[,†,‡]

[†]Department of Materials Science and Engineering, [‡]Center for Two-Dimensional and Layered Materials, and [⊥]Department of Electrical Engineering, The Pennsylvania State University, University Park, Pennsylvania 16802, United States, [§]Department of Materials Science and Engineering, The University of Texas at Dallas, Richardson, Texas 75080, United States, and [∥]US Army Research Laboratory, Adelphi, Maryland 20783, United States

ABSTRACT Tungsten diselenide (WSe_2) is a two-dimensional material that is of interest for next-generation electronic and optoelectronic devices due to its direct bandgap of 1.65 eV in the monolayer form and excellent transport properties. However, technologies based on this 2D material cannot be realized without a scalable synthesis process. Here, we demonstrate the first scalable synthesis of large-area, mono and few-layer WSe_2 *via* metal–organic chemical vapor deposition using tungsten hexacarbonyl ($W(CO)_6$) and dimethylselenium ($(CH_3)_2Se$). In addition to being intrinsically scalable, this technique allows for the precise control of the vapor-phase chemistry, which is unobtainable using more traditional oxide vaporization routes. We show that temperature, pressure, Se:W ratio, and substrate choice have a strong impact on the ensuing atomic layer structure, with optimized conditions yielding >8 μm size domains. Raman spectroscopy, atomic force microscopy (AFM), and cross-sectional transmission electron microscopy (TEM) confirm crystalline monoto-multilayer WSe_2 is achievable. Finally, TEM and vertical current/voltage transport provide evidence that a pristine van der Waals gap exists in WSe_2/graphene heterostructures.

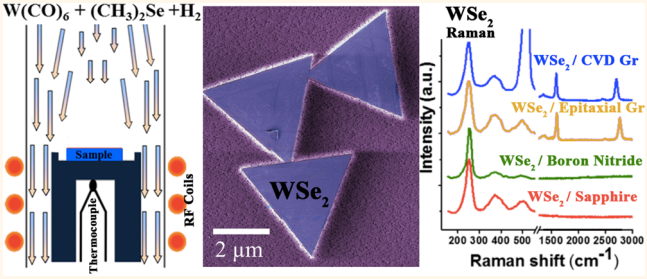

KEYWORDS: tungsten diselenide · WSe_2 · metal organic chemical vapor deposition (MOCVD) · transition-metal dichalcogenide · graphene · synthesis · two-dimensional (2D) materials

Beyond graphene, layered materials such as atomically thin transition-metal dichalcogenides (TMDs) have recently garnered interest due to their unique properties, including tunable bandgaps (~1–2 eV),[1–4] spin valley coupling,[5,6] and high on/off current ratios.[3] TMDs consist of one transition metal (M) and two chalcogen atoms (X) (*e.g.*, molybdenum disulfide (MoS_2), tungsten disulfide (WS_2), and tungsten diselenide (WSe_2)), and the majority of recent studies on these unique systems have been carried out on exfoliated material.[2,3,7] However, chemical vapor deposition of thick (>100 nm) TMD films has been successful using a variety of metal–organics ($W(CO)_6$, $Mo(CO)_6$, *etc.*)[8–10] and metal chlorides ($MoCl_5$, WCl_5, $WOCl_5$, $VOCl_5$)[8,11–13] combined with a wide range of chalcogen precursors.[8–13] These early processes, while not refined to synthesize atomically thin layers, provide important insight into precursor chemistries suitable for monolayer TMD synthesis and have led to a variety of reports on synthesis of monolayer MoS_2,[14–16] $MoSe_2$,[17–20] and WS_2.[21,22] Additionally, synthesis of WSe_2 has been reported *via* various techniques including pulsed laser deposition,[23] amorphous solid–liquid crystalline solid,[24] and powder vaporization.[25–27] These methods, while important for understanding the properties of monolayer TMDs, lack the control and reproducibility of the precursors needed for a truly scalable synthesis process. Thus, in order to advance technology, it is requisite to develop a scalable process that allows for more precise control of both the metal and chalcogen precursors for uniform nucleation and growth over large areas.

Here, we present the first metal–organic chemical vapor deposition (MOCVD) process for the synthesis of atomically thin WSe_2.

* Address correspondence to jrobinson@psu.edu.

Received for review December 22, 2014 and accepted January 27, 2015.

Published online January 27, 2015
10.1021/nn5073286

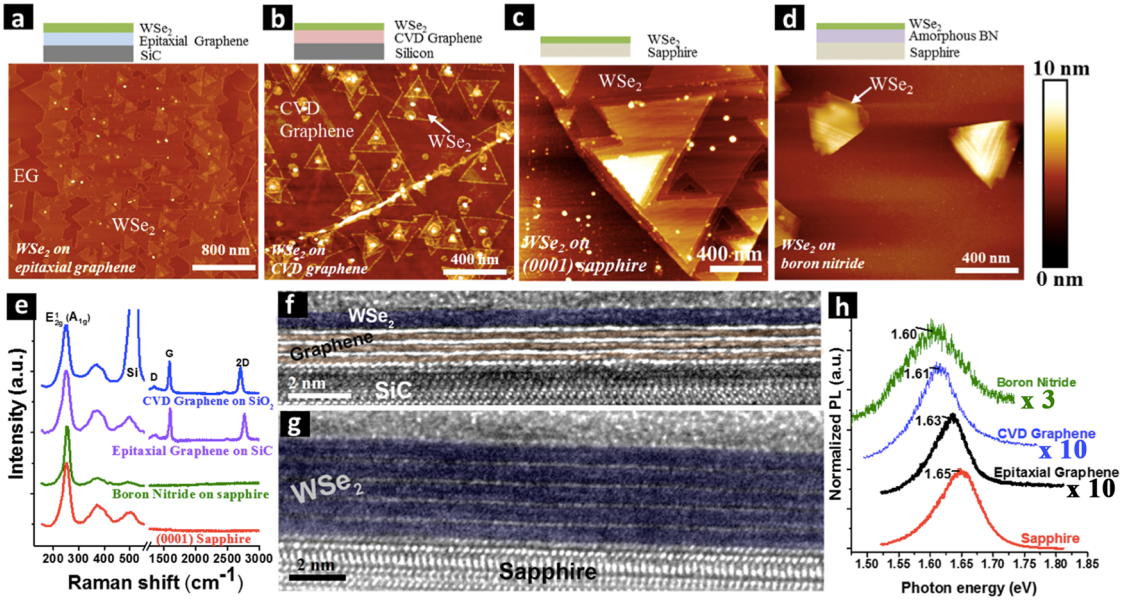

Figure 1. (a–d) AFM scans showing differences in the WSe_2 morphology when grown on (a) epitaxial graphene, (b) CVD graphene, (c) sapphire, and (d) boron nitride. (e) Raman spectra for WSe_2 growth on the various substrates showing similar quality. (f) Cross-sectional TEM showing high quality WSe_2 grown on epitaxial graphene. (g) Cross-sectional TEM of high quality, multilayer WSe_2 on sapphire. (h) Distinct shift in PL for synthesis of WSe_2 on the different substrates indicating the presence of strain.

We report synthesis on a wide variety of substrates including sapphire, graphene, and amorphous boron nitride (aBN) and provide evidence that the layer properties can be controlled by varying the Se:W ratio during growth. Characterization of the films using Raman spectroscopy, atomic force microscopy (AFM), and field emission scanning electron microscopy (FESEM) provide evidence that domain size, layer thickness, and morphology of the synthetic WSe_2 monolayers is of similar quality to exfoliated WSe_2. Growth conditions necessary to obtain large (5–8 μm) domains are reported, including the effect of temperature, pressure, and Se:W ratio. Conductive AFM and current–voltage (I–V) measurements of WSe_2/epitaxial graphene (EG) heterostructures provide evidence that the MOCVD-grown WSe_2 is of similar quality to WSe_2 grown by oxide powder vaporization,[28] and superior to exfoliated heterostructures,[29,30] suggesting a pristine interlayer gap is present between the WSe_2 and EG.

RESULTS AND DISCUSSION

The synthesis of WSe_2 was carried out *via* metal–organic chemical vapor deposition (MOCVD) in a vertical, cold-wall reactor system using tungsten hexacarbonyl ($W(CO)_6$) and dimethylselenium ($(CH_3)_2Se$) as the W and Se sources, respectively. Additional growth details are provided in the Methods and Supporting Information. While previous reports suggest adding small amounts of H_2 to promote WSe_2 growth,[31] synthesis using metal–organics requires the use of 100% hydrogen to minimize the carbon impurity incorporation from the $W(CO)_6$ and $(CH_3)_2Se$ precursors (see the Supporting Information).[32] Additionally, the precursor purity has a significant impact on the resultant film quality, where 99% pure $(CH_3)_2Se$ exhibits much higher carbon contamination compared to 99.99%, regardless of the H_2 concentration (see the Supporting Information).

Even with the potential for "van der Waals epitaxy", the choice of substrate clearly has a significant impact on the morphology of atomically thin WSe_2 domains. This is apparent in Figure 1a–d, where AFM confirms that epitaxial graphene (Figure 1a), CVD graphene (Figure 1b), sapphire (Figure 1c), and amorphous boron nitride (Figure 1d) substrates all yield distinct morphologies and thicknesses when grown under the same conditions. This suggests that there may be significant interaction between the WSe_2 and substrate during synthesis. Epitaxial and CVD graphene (Figure 1a,b) yield the highest nucleation density of monolayer WSe_2 domains, while amorphous boron nitride yields the lowest nucleation density with a strong preference for vertical (3D) growth of WSe_2 *versus* lateral (2D) growth. The presence of reactive defects and wrinkles in graphene is known to provide low energy nucleation sites for the growth of MoS_2.[26] This is also the case in this work, where graphene defects and surface contamination from the transfer process for CVD graphene results in a high density of 3D-WSe_2 structures at the center of most of the 2D-WSe_2 domains. Growth on sapphire substrates yields the largest domains (5–8 μm) with additional layers growing from edge sites or defect sites on the monolayer. This is further supported with Raman spectroscopy mapping (Supporting Information). This suggests that the sticking coefficient for Se and W atoms on the surface of

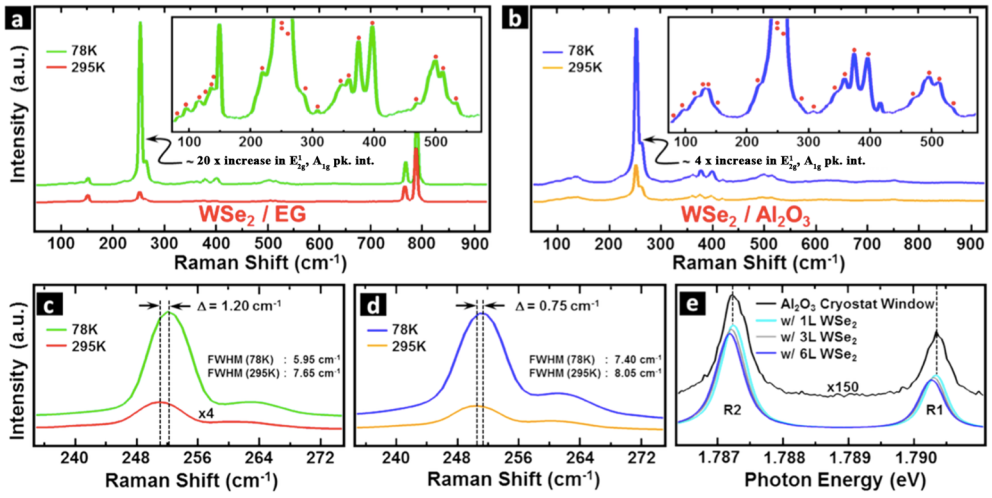

Figure 2. (a) Raman spectra over a wide range for WSe_2 grown on EG at 295 K (red) and 78 K (green) displaying 20× increase in signal at 78 K. (b) Raman spectra for WSe_2 grown on sapphire at 295 K (yellow) and 78 K (blue) displaying 4× increase in signal at 78 K. Peak shift and fwhm for E^1_{2g} and A_{1g} with respect to temperature for WSe_2 grown on EG (c) and sapphire (d). (e) Effect of WSe_2 layer count on the R1 and R2 peaks for sapphire.

sapphire is greater than the other substrates, providing a means to achieve larger triangles through diffusion of source material across the substrate surface. Finally, the presence of the E^1_{2g} and A_{1g} peaks of WSe_2 in Raman spectroscopy (Figure 1e) are observed, confirming the presence of WSe_2.[33] Similar to previous reports,[26,28] the synthesis of the WSe_2 on graphene to form a van der Waals heterostructure does not appear to significantly degrade the underlying graphene based on the minimal "D" peak at 1360 cm^{-1} in the Raman spectra.

Metal−organic CVD yields crystalline WSe_2 atomic layers with a tunable optical bandgap based on substrate choice. Cross-sectional transmission electron microscopy (TEM) of WSe_2 on epitaxial graphene and sapphire (Figure 1f and g) confirm the presence of crystalline WSe_2 with pristine interfaces. In the case of growth on epitaxial graphene, TEM confirms the presence of three layers of epitaxial graphene and a single monolayer of WSe_2, with a clean interface and no observable defects. In contrast, for the case of multilayer WSe_2 on sapphire, TEM reveals some disorder at the WSe_2/sapphire interface suggesting a reaction during growth, which is similar to that found for WSe_2 films synthesized *via* selenium−oxygen ion exchange of tungsten oxide.[34] Interestingly, the normalized photoluminescence peak position (Figure 1h), corresponding to the optical bandgap of WSe_2, shifts from the theoretically predicted 1.65 eV on sapphire to 1.63, 1.62, and finally 1.60 eV for WSe_2 on epitaxial graphene, CVD graphene, and amorphous boron nitride (aBN), respectively. The shift and reduction in intensity for WSe_2 on aBN is likely due to the formation of few-layer WSe_2. This is evident from the very weak signal (low signal-to-noise ratio) due to the transition from a direct to indirect bandgap material above a single layer. The shift in the peak for epitaxial and CVD graphene may be from strain, doping, or both.[35] In the case of CVD graphene, Raman spectroscopy provides evidence that, while no additional defects are formed in the graphene during growth, there is a significant amount of strain introduced into the graphene following the deposition of WSe_2 (see the Supporting Information). Therefore, it is likely that the WSe_2 is also strained due to interlayer interactions, which ultimately reduce the bandgap by 30 meV.[36,37]

Temperature-dependent Raman and phosphorescence spectroscopy reveals significant variations in the quality of the WSe_2 based on the substrate choice and indicates graphene may be an ideal substrate for high quality TMD synthesis. Raman spectroscopy has been utilized extensively to investigate bulk[38,39] and few-layer[25,40−47] WSe_2 at room temperature, while only one study has been carried out at low temperature over the spectral range of 230−270 cm^{-1}.[39] Here, we investigated low-temperature Raman spectroscopy on WSe_2 grown on sapphire and epitaxial graphene substrates. Low-temperature Raman spectroscopy resolves a number of modes difficult to observe at room temperature, with peaks being more distinguishable on EG compared to sapphire (Figure 2a,b) at 78 K. By magnifying different segments of the spectra, a total of 21 peaks (inset of Figure 2a,b) associated with WSe_2 are identifiable (Table 1, Supporting Information). A blue shift and considerable enhancement in the intensity are observed at 78 K when comparing the spectra for EG (Figure 2a,c) and sapphire (Figure 2b,d) at 78 and 295 K, which is attributed to the tuning of the A′ and/or B′ exciton to resonance with the exciting laser.[46] A sharpening of the fwhm of the E^1_{2g} and A_{1g} peaks at 78 K for both growth substrates was also observed (Figure 2c,d); however, the fwhm for WSe_2 on EG is significantly narrower, indicating an improvement in the WSe_2 growth on EG. Furthermore, there is a

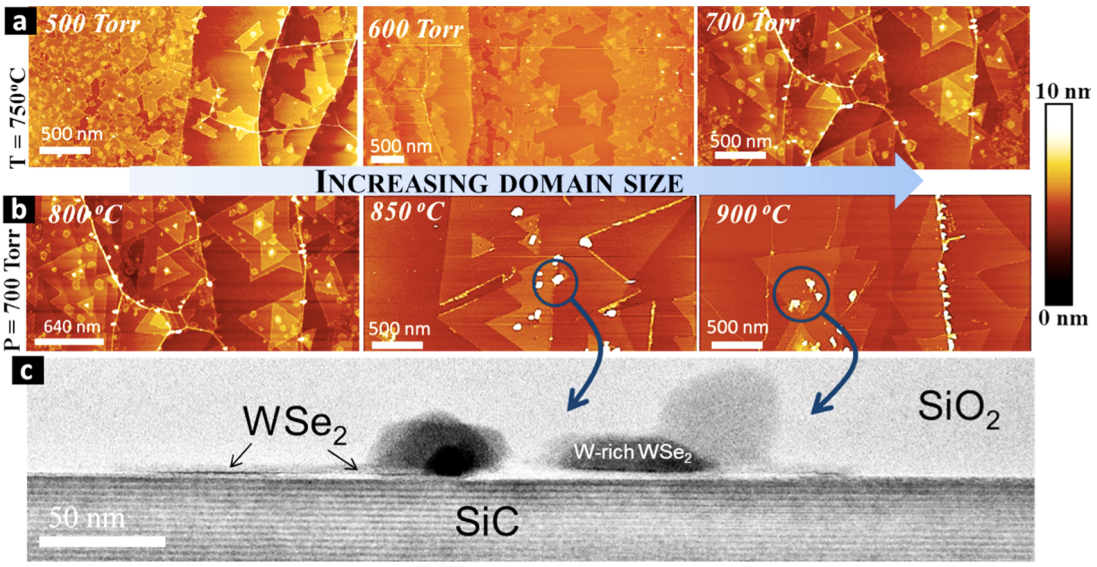

Figure 3. (a,b) AFM of WSe_2 on EG showing increased domain size with increasing temperature and pressure. (c) Cross-sectional TEM of WSe_2 on EG showing particulates identified as W-rich WSe_2.

significant difference in the peak intensity enhancement (EG ≫ sapphire) across the sample, also indicating improved crystal quality on EG even though the room-temperature Raman and PL are quenched compared to sapphire. Additional analysis of spectral features originating from the sapphire substrate (R1 and R2 phosphorescence peaks) indicates a peak position dependence on WSe_2 layer count (Figure 2e). This shift in the peaks is potentially due to a built-in stress at the sapphire/TMD interface.[48] These observations coincide with the TEM results showing some disorder at the WSe_2/sapphire interface (Supporting Information).

Growth conditions, including temperature and total pressure, have a strong impact on the overall domain size, shape, and nucleation density. Focusing on sapphire and epitaxial graphene, we find that the WSe_2 domain size increases with increased temperature and pressure. This is shown for growth on epitaxial graphene in Figure 3a,b. While the temperature is constant at 750 °C, and the Se:W ratio is 100, the nucleation density decreases while the domain size increases from ~250 nm to 700 nm when the total pressure is increased from 500 to 700 Torr. Likewise, when the pressure is constant at 650 Torr, and the Se:W ratio remains 100, an increase in temperature of 100 °C (800 → 900 °C) yields a 200% increase in domain size (700 nm →1.5 μm). The growth on sapphire substrates yields similar results. Synthesis at high pressure also results in the formation of particulates on the sample surface (Figure 3b), which were subsequently identified as W-rich WSe_2 *via* cross-sectional TEM (Figure 3c and Supporting Information). The presence of such particles indicates a deficiency of Se at the growth surface during the deposition of WSe_2 and therefore merited an investigation into the impact of the selenium-to-tungsten (Se:W) ratio.

As a result, the Se:W ratio is a critical factor in controlling defect formation in WSe_2. This is evident in Figure 4a, where a surface plot of temperature and pressure *versus* Se:W ratio clearly demonstrates that domain size increases significantly as the Se:W ratio is increased to 800. Additionally, as the Se:W ratio increases, there is a decrease in the density of W-rich WSe_2 particulates. This further supports the TEM analysis determining the particulates to be due to an imbalance in Se:W ratio. This led to a more detailed analysis of Se:W ratio and included "extreme" ratios. Figure 4b plots the domain size as a function of Se:W ratio. Extreme MOCVD ratios of up to 20000 Se:W allows for a dramatic increase in domain size from 1 to 5 μm. Pushing the Se:W ratio to high values through a reduction in $W(CO)_6$ also leads to a decrease in the amount of nucleation sites and a reduced tendency to form Se vacancies which lead to secondary nucleation sites. Above a ratio of 20000, however, the domain size begins to decrease again, suggesting that there is an ideal ratio for large domain growth. This reduction in ratio is also accompanied by significant deposition of selenium on the sidewalls of the furnace suggesting that selenium vapor saturation occurs and begins to reverse the thermodynamic driving force for formation of WSe_2 from W and Se. We note that these ratios can vary based on reactor design.

Beyond temperature, pressure, and precursor ratios, the total flow through the system can also have a large impact. Parts c–e of Figure 4 demonstrate the impact of total flow on the domain size and shape. Temperature, pressure, and Se:W ratio were held constant at optimized conditions (800 °C, 700 Torr, and 20,000 Se:W), while the total flow through the system was increased from 100 to 500 sccm. A total flow of 250 sccm yields 8 μm WSe_2 domains, while higher flow rates of 500 sccm result in a

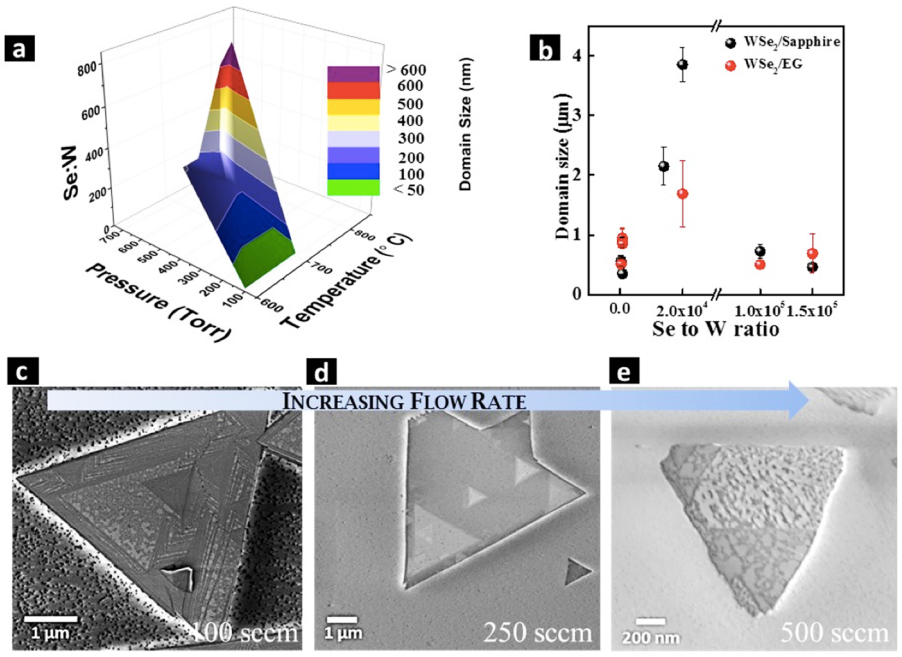

Figure 4. (a) Plot of temperature, pressure, and low (<1000) Se:W flux ratios as a function of domain size for sapphire substrates showing the impact of Se:W flux ratio on domain size. (b) Plot of extreme Se:W flux ratios as a function of domain size for both sapphire and epitaxial graphene indicating an optimum Se:W flux ratio around 2.0×10^4. (c–e) FESEM showing the change in domain size as a function of total flow rate.

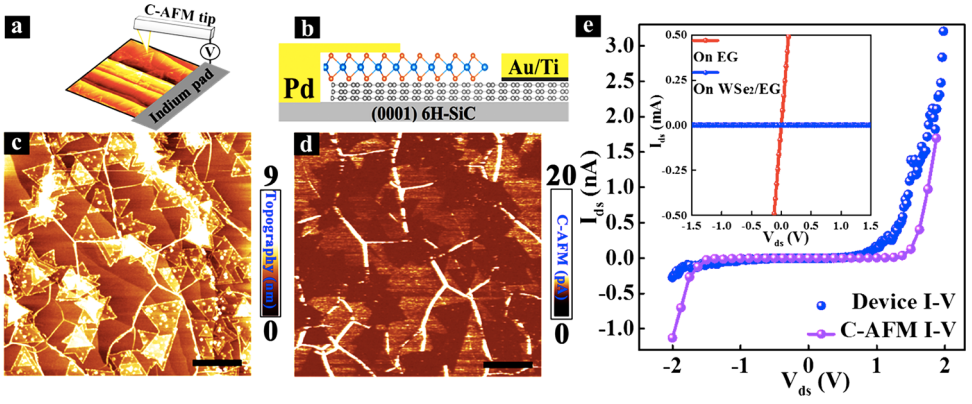

Figure 5. a() Conductive-AFM setup with an indium pad and Pt-coated AFM tip, which were used as the ground and the source for the measurement. (b) Schematic structure (side view) of 1L WSe_2-EG diode using Au/Ti and Pt as source and drain contact, respectively. (c) WSe_2 on EG AFM correlated with (d) conductive AFM mapping. (e) WSe_2–EG diodes display a thermionic emission-like tunnel current turning on before 2 V, while WSe_2 grown on EG as a barrier reduced the current by an order of 6 (inset of e).

decrease in domain size and less defined WSe_2 edges. Increased total flow from 100 to 250 sccm increases the gas velocity in the system, which may reduce gas phase depletion of sources upstream of the substrate thereby leading to an increased gas flux at the sample surface and higher lateral growth rates. However, further increasing the total gas flow rate from 250 to 500 sccm leads to a decrease in domain size, suggesting that the higher gas velocities do not allow sufficient time for source decomposition and reaction.

In addition to synthesis of WSe_2, the syntheses of van der Waals heterostructures are also of increasing importance in the advancement of the field. Synthesis of WSe_2 on graphene *via* MOCVD leads to a high-quality heterostructure. Conductive atomic force microscopy (C-AFM) provides a direct nondestructive way to probe the electronic properties of WSe_2/EG heterostructures on the nanoscale and explore the utility of the materials for electronic and optoelectronic applications (Figure 5a,c,d). Comparison of AFM surface topography and conductivity acquired at $V_{bias} = +$ 0.8 V (Polarity is from the AFM tip to the sample) clearly indicates that a barrier to transport exists in the heterojunction regions. Current mapping reveals that both the 1L WSe_2 and multilayer WSe_2 are uniformly resistive, while high conductivity is observed on the graphene area with graphene wrinkles (bright stripes in Figure 5c) exhibiting enhanced conduction through the AFM tip.

Vertical diode structures (Figure 5b,e) confirm the presence of a tunnel barrier to vertical transport created by the WSe_2 (Figure 5e). The barrier persists under an increasing V_{bias} up to ± 2 V prior to turn-on, while the area only having graphene clearly exhibits linear $I-V$ behavior (Inset Figure 5e). A resistance of $\sim 10^{10}$ Ω prior to turn-on suggests an interlayer gap exists at the WSe_2/EG interface. This work is similar to that found for oxide-powder vaporization synthesis of WSe_2 and MoS_2 on graphene,[26,28] and indicates that the MOCVD-grown van der Waals heterostructures are a promising route for scalable synthesis of such structures.

CONCLUSION

In summary, a process for metal−organic chemical vapor deposition was developed to synthesize highly crystalline monolayer and multilayer WSe_2 and WSe_2/graphene heterostructures. This is the first known report to achieve monolayer control of large domain TMD structures *via* MOCVD, and this process allows for excellent control over the process conditions which is necessary to tune domain size, shape, and nucleation density. Synthesis *via* MOCVD offers a highly scalable process with precise control over the gas-phase chemistry, which cannot be accomplished using powder vaporization methods.

METHODS

Synthesis and Characterization. Tungsten selenide was synthesized using tungsten hexacarbonyl (Sigma-Aldrich 99.99%) and dimethylselenium precursors (SAFC (99.99%) or STREM Chemical (99%)) in a vertical cold wall reactor with an induction heated susceptor as described previously.[49] The precursors were transported into the system *via* a bubbler manifold allowing for independent control over each precursor concentration. The carrier gas included H_2/N_2 mixtures with 100% H_2 being optimal. The samples were heated to 500 °C at 80 °C/min and annealed for 15 min to drive off any water vapor. Samples were then heated to growth temperatures ranging from 600 to 900 °C at 80 °C/min. Upon reaching growth temperature the tungsten hexacaronyl and dimethylselenium were introduced into the reaction chamber. Growth took place at total pressures from 100 to 700 Torr and growth times were 30 min. The Se and W concentrations were varied by changing the H_2 carrier gas flow rate from 5 to 35 sccm at bubbler pressures of 760 Torr for Se and 700 Torr for W and both bubblers were maintained at a temperature of 23 °C. Samples were cooled to room temperature after the growth step was complete. Epitaxial graphene is grown on diced SiC wafers *via* sublimation of silicon from 6H-SiC (0001) at 1700 °C for 15 min under 1 Torr Ar background pressure;[26] CVD graphene was prepared *via* a catalytic CVD method on 25 μm 99.999% pure Cu foils at 1050 °C, 1 Torr and transferred onto SiO_2/Si *via* PMMA membrane.[50] The BN was deposited on sapphire substrates *via* a pulse laser deposition (PLD) technique. [51] The as-grown samples were characterized using Raman spectroscopy, atomic force microscopy (AFM), and transmission electron microscopy (TEM). A WITec CRM200 confocal Raman microscope with 488 and 633 nm laser wavelengths was utilized for structural characterization at room temperature. A BRUKER Dimension 3100 with a scan rate of 0.75−1 Hz was utilized for the AFM measurements. Scanning electron microscopy was carried out using a Zeiss MERLIN FESEM. TEM cross-sectional samples were made by a FEI Nova 200 dual-beam FIB/SEM with lift-out method. A carbon layer was deposited on the WSe_2 surface to avoid electron charging. In FIB, SiO_2 and Pt layers were deposited to protect the region of interest during focused ion beam milling. A JEOL ARM200F transmission electron microscope operated at 200 kV with a probe aberration corrector was used for high-resolution TEM (HRTEM) imaging and energy-dispersive X-ray spectroscopy (EDS) analysis.

The low-temperature Raman spectroscopy was accomplished with a WITec Alpha 300RA system using a 2.54 eV laser excitation energy. The spectra were measured in the backscattering configuration using a 63× objective and either a 600 or 1800 grooves/mm grating. Incident laser power was adjusted in order to keep the power density at 2.8 mW/um^2 for single spectra data. This laser power was kept sufficiently low to avoid significant heat-related affects in the Raman signatures even for spot measurements lasting up to 5 min. The 78 K measurements were performed using a Janis Research Supertran ST-500-UC system mounted to a motorized stage. The top flange of this continuous flow cryostat was designed to accommodate a 15 mm diameter x 0.3 mm thick *c*-axis UV quality sapphire window allowing for the use of high numerical aperture objectives (≥0.6), and a lateral resolution ≤400 nm for the wavelength of light used in this work. Raman images were developed over several 20 × 20 μm regions using a 250 nm grid spacing with a 1 s integration time. Regions of interest were identified from these maps for which single spectra were obtained using a 2 s integration time and 60 accumulations.

Device Fabrication and Other Measured I−V curves. The vertical diode was fabricated with electron beam lithography and lift-off of evaporated metal contacts. In the first step, the graphene contact is patterned and developed with electron beam (e-beam) lithography. Subsequently, metal contacts Ti/Au (10 nm/40 nm) are deposited with low pressure electron beam evaporation (10^{-7} Torr) after a oxygen plasma treatment to reduce the contact resistance (45 s at 100 W, 50 sccm He, 150 sccm O_2 at 500 mTorr). Then, a layer of 30 nm Al_2O_3 is deposited conformally over the entire substrate with atomic layer deposition (ALD), which serves as a protective layer for subsequent processing steps and a passivation layer. ALD deposited Al_2O_3 capping layer has been reported as an effective film to substantially improve carrier mobility in 2D materials. In the second e-beam lithography step, a pattern of etch regions are defined, including an opening on the Ti/Au pads, and regions for the later WSe_2 contacts. The Al_2O_3 capping layer on these regions are first removed with hydrofluoric acid followed by oxygen plasma etching to remove the monolayer WSe_2 and few layers of graphene. This step prevents shorting through the underlying graphene layer after depositing the WSe_2 contacts. In the third e-beam step, the WSe_2 contact pads and thin lines are defined, and the Al_2O_3 layer on the WSe_2 triangular sheets is removed by hydrofluoric acid prior to the metal deposition. Then 50 nm thick palladium (Pd) layer is deposited by electron beam evaporation at 10^{-7} Torr. The high work function Pd contacts with WSe_2 have been reported to produce a smaller Schottky barrier and many orders higher current density compared to Ti/Au contacts.

Conflict of Interest: The authors declare no competing financial interest.

Acknowledgment. We thank N. R. Glavin and A. A. Voevodin of the Nanoelectronic Materials Branch, Air Force Research Laboratory, Wright-Patterson AFB, Dayton, OH, for providing BN/sapphire substrates for synthesis. The work at Penn State and UT Dallas was supported by the Center for Low Energy Systems Technology (LEAST), one of six centers supported by the STARnet phase of the Focus Center Research Program (FCRP), a Semiconductor Research Corporation (SRC) program sponsored by MARCO and DARPA. Work at UT Dallas was also supported by the Southwest Academy on Nanoelectronics (SWAN), a SRC center sponsored by the Nanoelectronics Research Initiative and NIST. The work at the U.S. Army Research

Laboratory (ARL) was supported by the Director's Strategic Initiative (DSI) program on interfaces in stacked 2D atomic layered materials. Device fabrication was partially supported by the Pennsylvania State University Materials Research Institute Nanofabrication Laboratory and the National Science Foundation Cooperative Agreement No. ECS-0335765.

Supporting Information Available: Figures S1–S5 and Tables T1 and T2. This material is available free of charge *via* the Internet at http://pubs.acs.org

REFERENCES AND NOTES

1. Mak, K. F.; Lee, C.; Hone, J.; Shan, J.; Heinz, T. F.; Mak, K.; Lee, C.; Hone, J.; Shan, J.; Heinz, T. Atomically Thin MoS_2: A New Direct-Gap Semiconductor. *Phys. Rev. Lett.* **2010**, *105*, 2–5.
2. Liu, W.; Kang, J.; Sarkar, D.; Khatami, Y.; Jena, D.; Banerjee, K. Role of Metal Contacts in Designing High-Performance Monolayer N-Type WSe_2 Field Effect Transistors. *Nano Lett.* **2013**, *13*, 1983–1990.
3. Fang, H.; Chuang, S.; Chang, T. C.; Takei, K.; Takahashi, T.; Javey, A. High Performance Single Layered WSe_2 P-FETs with Chemically Doped Contacts. *Nano Lett.* **2012**, *12*, 3788–3792.
4. Baugher, B. W. H.; Churchill, H. O. H.; Yang, Y.; Jarillo-Herrero, P. Optoelectronic Devices Based on Electrically Tunable P–N Diodes in a Monolayer Dichalcogenide. *Nat. Nanotechnol.* **2014**, *9*, 262–267.
5. Zeng, H.; Liu, G.-B.; Dai, J.; Yan, Y.; Zhu, B.; He, R.; Xie, L.; Xu, S.; Chen, X.; Yao, W.; *et al.* Optical Signature of Symmetry Variations and Spin-Valley Coupling in Atomically Thin Tungsten Dichalcogenides. *Sci. Rep.* **2013**, *3*, 1608.
6. Xiao, D.; Liu, G.-B.; Feng, W.; Xu, X.; Yao, W. Coupled Spin and Valley Physics in Monolayers of MoS_2 and Other Group-VI Dichalcogenides. *Phys. Rev. Lett.* **2012**, *108*, 196802.
7. Zhao, W.; Ghorannevis, Z.; Chu, L.; Toh, M.; Kloc, C.; Tan, P.; G, E. Evolution of Electronic Structure in Thin Sheets of WS_2 and WSe_2. *ACS Nano* **2013**, *7*, 791–797.
8. Boscher, N. D.; Blackman, C. S.; Carmalt, C. J.; Parkin, I. P.; Prieto, A. G. Atmospheric Pressure Chemical Vapour Deposition of Vanadium Diselenide Thin Films. *Appl. Surf. Sci.* **2007**, *253*, 6041–6046.
9. Chung, J.-W.; Dai, Z. R.; Ohuchi, F. S. WS_2 Thin Films by Metal Organic Chemical Vapor Deposition. *J. Cryst. Growth* **1998**, *186*, 137–150.
10. Hofmann, W. K. Thin Films of Molybdenum and Tungsten Disulphides by Metal Organic Chemical Vapour Deposition. *J. Mater. Sci.* **1988**, *23*, 3981–3986.
11. Boscher, N. D.; Carmalt, C. J.; Palgrave, R. G.; Gil-Tomas, J. J.; Parkin, I. P. Atmospheric Pressure CVD of Molybdenum Diselenide Films on Glass. *Chem. Vap. Depos.* **2006**, *12*, 692–698.
12. Carmalt, C. J.; Parkin, I. P.; Peters, E. S. Atmospheric Pressure Chemical Vapour Deposition of WS_2 Thin Films on Glass. *Polyhedron* **2003**, *22*, 1499–1505.
13. Imanishi, N. Synthesis of MoS_2 Thin Film by Chemical Vapor Deposition Method and Discharge Characteristics as a Cathode of the Lithium Secondary Battery. *J. Electrochem. Soc.* **1992**, *139*, 2082.
14. Lee, Y.-H.; Yu, L.; Wang, H.; Fang, W.; Ling, X.; Shi, Y.; Lin, C.-T.; Huang, J.-K.; Chang, M.-T.; Chang, C.-S.; *et al.* Synthesis and Transfer of Single-Layer Transition Metal Disulfides on Diverse Surfaces. *Nano Lett.* **2013**, *13*, 1852–1857.
15. Schmidt, H.; Wang, S.; Chu, L.; Toh, M.; Kumar, R.; Zhao, W.; Neto, a H. C.; Martin, J.; Adam, S.; Özyilmaz, B.; *et al.* Transport Properties of Monolayer MoS_2 Grown by Chemical Vapor Deposition. *Nano Lett.* **2014**, *14*, 1909–1913.
16. Yu, Y.; Li, C.; Liu, Y.; Su, L.; Zhang, Y.; Cao, L. Controlled Scalable Synthesis of Uniform, High-Quality Monolayer and Few-Layer MoS_2 Films. *Sci. Rep.* **2013**, *3*, 1866.
17. Kong, D.; Wang, H.; Cha, J. J.; Pasta, M.; Koski, K. J.; Yao, J.; Cui, Y. Synthesis of MoS_2 and $MoSe_2$ Films with Vertically Aligned Layers. *Nano Lett.* **2013**, *13*, 1341–1347.
18. Shim, G. W.; Yoo, K.; Seo, S.-B.; Shin, J.; Jung, D. Y.; Kang, I.-S.; Ahn, C. W.; Cho, B. J.; Choi, S.-Y. Large-Area Single-Layer $MoSe_2$ and Its van der Waals Heterostructures. *ACS Nano* **2014**, *8*, 6655–6662.
19. Wang, X.; Gong, Y.; Shi, G.; Chow, W. L.; Keyshar, K.; Ye, G.; Vajtai, R.; Lou, J.; Liu, Z.; Ringe, E.; *et al.* Chemical Vapor Deposition Growth of Crystalline Monolayer $MoSe_2$. *ACS Nano* **2014**, *8*, 5125–5131.
20. Chang, Y.-H.; Zhang, W.; Zhu, Y.; Han, Y.; Pu, J.; Chang, J.-K.; Hsu, W.-T.; Huang, J.-K.; Hsu, C.-L.; Chiu, M.-H.; *et al.* Monolayer $MoSe_2$ Grown by Chemical Vapor Deposition for Fast Photodetection. *ACS Nano* **2014**, *8*, 8582–8590.
21. Elías, A. L.; Perea-López, N.; Castro-Beltrán, A.; Berkdemir, A.; Lv, R.; Feng, S.; Long, A. D.; Hayashi, T.; Kim, Y. A.; Endo, M.; *et al.* Controlled Synthesis and Transfer of Large-Area WS_2 Sheets: From Single Layer to Few Layers. *ACS Nano* **2013**, *7*, 5235–5242.
22. Tongay, S.; Fan, W.; Kang, J.; Park, J.; Koldemir, U.; Suh, J.; Narang, D. S.; Liu, K.; Ji, J.; Li, J.; *et al.* Tuning Interlayer Coupling in Large-Area Heterostructures with CVD-Grown MoS_2 and WS_2 Monolayers. *Nano Lett.* **2014**, *14*, 3185–3190.
23. Grigoriev, S. N.; Fominski, V. Y.; Gnedovets, A. G.; Romanov, R. I. Experimental and Numerical Study of the Chemical Composition of WSex Thin Films Obtained by Pulsed Laser Deposition in Vacuum and in a Buffer Gas Atmosphere. *Appl. Surf. Sci.* **2012**, *258*, 7000–7007.
24. Bozheyev, F.; Friedrich, D.; Nie, M.; Rengachari, M.; Ellmer, K. Preparation of Highly (001)-Oriented Photoactive Tungsten Diselenide (WSe_2) Films by an Amorphous Solid-Liquid-Crystalline Solid (aSLcS) Rapid-Crystallization Process. *Phys. Status Solidi* **2014**, *211*, 2013–2019.
25. Huang, J.-K.; Pu, J.; Hsu, C.-L.; Chiu, M.-H.; Juang, Z.-Y.; Chang, Y.-H.; Chang, W.-H.; Iwasa, Y.; Takenobu, T.; Li, L.-J. Large-Area Synthesis of Highly Crystalline WSe_2 Monolayers and Device Applications. *ACS Nano* **2014**, *8*, 923–930.
26. Lin, Y.-C.; Lu, N.; Perea-Lopez, N.; Li, J.; Lin, Z.; Peng, X.; Lee, C. H.; Sun, C.; Calderin, L.; Browning, P. N.; *et al.* Direct Synthesis of van der Waals Solids. *ACS Nano* **2014**, *8*, 3715–3723.
27. Xu, K.; Wang, Z.; Du, X.; Safdar, M.; Jiang, C.; He, J. Atomic-Layer Triangular WSe_2 Sheets: Synthesis and Layer-Dependent Photoluminescence Property. *Nanotechnology* **2013**, *24*, 465705.
28. Lin, Y.-C.; Chang, C.-Y. S.; Ghosh, R. K.; Li, J.; Zhu, H.; Addou, R.; Diaconescu, B.; Ohta, T.; Peng, X.; Lu, N. Atomically Thin Heterostructures Based on Single-Layer Tungsten Diselenide and Graphene. *Nano Lett.* **2014**, *14*, 6936–6941.
29. Haigh, S. J.; Gholinia, A.; Jalil, R.; Romani, S.; Britnell, L.; Elias, D. C.; Novoselov, K. S.; Ponomarenko, L. A.; Geim, A. K.; Gorbachev, R. Cross-Sectional Imaging of Individual Layers and Buried Interfaces of Graphene-Based Heterostructures and Superlattices. *Nat. Mater.* **2012**, *11*, 764–767.
30. Lee, C.-H.; Lee, G.-H.; van der Zande, A. M.; Chen, W.; Li, Y.; Han, M.; Cui, X.; Arefe, G.; Nuckolls, C.; Heinz, T. F.; *et al.* Atomically Thin P–N Junctions with van der Waals Heterointerfaces. *Nat. Nanotechnol.* **2014**, *9*, 676–681.
31. Huang, J.-K. K.; Pu, J.; Hsu, C.-L. L.; Chiu, M.-H. H.; Juang, Z.-Y. Y.; Chang, Y.-H. H.; Chang, W.-H. H.; Iwasa, Y.; Takenobu, T.; Li, L.-J. J. Large-Area Synthesis of Highly Crystalline WSe_2 Monolayers and Device Applications. *ACS Nano* **2014**, *8*, 923–930.
32. Haigh, J.; Burkhardt, G.; Blake, K. Thermal Decomposition of Tungsten Hexacarbonyl in Hydrogen, the Production of Thin Tungsten-Rich Layers, and Their Modification by Plasma Treatment. *J. Cryst. Growth* **1995**, *155*, 266–271.
33. Terrones, H.; Del Corro, E.; Feng, S.; Poumirol, J. M.; Rhodes, D.; Smirnov, D.; Pradhan, N. R.; Lin, Z.; Nguyen, M. A. T.; Elías, A. L.; *et al.* New First Order Raman-Active Modes in Few Layered Transition Metal Dichalcogenides. *Sci. Rep.* **2014**, *4*, 4215.
34. Browning, P.; Eichfeld, S.; Zhang, K.; Hossain, L.; Lin, Y.-C.; Wang, K.; Lu, N.; Waite, A. R.; Voevodin, A. A.; Kim, M.; *et al.* Large-Area Synthesis of WSe_2 from WO_3 by

Selenium−oxygen Ion Exchange. *2D Mater.* **2015**, *2*, 014003.
35. Castellanos-Gomez, A.; Rolda, R.; Cappelluti, E.; Buscema, M. Local Strain Engineering in Atomically Thin MoS_2. *Nano Lett.* **2013**, *13*, 5361–5366.
36. Scalise, E.; Houssa, M.; Pourtois, G.; Afanas'ev, V.; Stesmans, A. Strain-Induced Semiconductor to Metal Transition in the Two-Dimensional Honeycomb Structure of MoS_2. *Nano Res.* **2012**, *5*, 43–48.
37. Castellanos-Gomez, A.; Roldán, R.; Cappelluti, E.; Buscema, M.; Guinea, F.; van der Zant, H. S. J.; Steele, G. A. Local Strain Engineering in Atomically Thin MoS_2. *Nano Lett.* **2013**, *13*, 5361–5366.
38. Verble, J.; Wieting, T. Lattice Mode Degeneracy in MoS_2 and Other Layer Compounds. *Phys. Rev. Lett.* **1970**, *25*, 362–365.
39. Mead, D.; Irwin, J. Long Wavelength Optic Phonons in WSe_2. *Can. J. Phys.* **1977**, *55*, 379–382.
40. Li, H.; Lu, G.; Wang, Y.; Yin, Z.; Cong, C.; He, Q.; Wang, L.; Ding, F.; Yu, T.; Zhang, H. Mechanical Exfoliation and Characterization of Single- and Few-Layer Nanosheets of WSe_2, TaS_2, and $TaSe_2$. *Small* **2013**, *9*, 1974–1981.
41. Tonndorf, P.; Schmidt, R.; Böttger, P.; Zhang, X.; Börner, J.; Liebig, A.; Albrecht, M.; Kloc, C.; Gordan, O.; Zahn, D. R. T.; *et al.* Photoluminescence Emission and Raman Response of Monolayer MoS_2, $MoSe_2$, and WSe_2. *Opt. Express* **2013**, *21*, 4908–4916.
42. Zhao, Y.; Luo, X.; Li, H.; Zhang, J.; Araujo, P. T.; Gan, C. K.; Wu, J.; Zhang, H.; Quek, S. Y.; Dresselhaus, M. S.; *et al.* Interlayer Breathing and Shear Modes in Few-Trilayer MoS_2 and WSe_2. *Nano Lett.* **2013**, *13*, 1007–1015.
43. Sahin, H.; Tongay, S.; Horzum, S.; Fan, W.; Zhou, J.; Li, J.; Wu, J.; Peeters, F. M. Anomalous Raman Spectra and Thickness-Dependent Electronic Properties of WSe_2. *Phys. Rev. B - Condens. Matter Mater. Phys.* **2013**, *87*, 165409.
44. Zhao, W.; Ghorannevis, Z.; Amara, K. K.; Pang, J. R.; Toh, M.; Zhang, X.; Kloc, C.; Tan, P. H.; Eda, G. Lattice Dynamics in Mono- and Few-Layer Sheets of WS_2 and WSe_2. *Nanoscale* **2013**, *5*, 9677–9683.
45. Luo, X.; Zhao, Y.; Zhang, J.; Toh, M.; Kloc, C.; Xiong, Q.; Quek, S. Y. Effects of Lower Symmetry and Dimensionality on Raman Spectra in Two-Dimensional WSe_2. *Phys. Rev. B* **2013**, *88*, 195313.
46. Del Corro, E.; Terrones, H.; Elias, A.; Fantini, C.; Feng, S.; Nguyen, M. A.; Mallouk, T. E.; Terrones, M.; Pimenta, M. A. Excited Excitonic States in 1L, 2L, 3L, and Bulk WSe_2 Observed by Resonant Raman Spectroscopy. *ACS Nano* **2014**, *8*, 9629–9635.
47. Ribeiro-Soares, J.; Almeida, R. M.; Barros, E. B.; Araujo, P. T.; Dresselhaus, M. S.; Cançado, L. G.; Jorio, A. Group Theory Analysis of Phonons in Two-Dimensional Transition Metal Dichalcogenides. *Phys. Rev. B* **2014**, *90*, 115438.
48. Forman, R. A.; Piermarini, G. J.; Barnett, J. D.; Block, S. Pressure Measurement Made by the Utilization of Ruby Sharp-Line Luminescence. *Science* **1972**, *176*, 284–285.
49. Brom, J. E.; Ke, Y.; Du, R.; Won, D.; Weng, X.; Andre, K.; Gagnon, J. C.; Mohney, S. E.; Li, Q.; Chen, K.; *et al.* Structural and Electrical Properties of Epitaxial Bi_2Se_3 Thin Films Grown by Hybrid Physical-Chemical Vapor Deposition. *Appl. Phys. Lett.* **2012**, *100*, 162110.
50. Howsare, C. A.; Weng, X.; Bojan, V.; Snyder, D.; Robinson, J. A. Substrate Considerations for Graphene Synthesis on Thin Copper Films. *Nanotechnology* **2012**, *23*, 135601.
51. Glavin, N. R.; Jespersen, M. L.; Check, M. H.; Hu, J.; Hilton, A. M.; Fisher, T. S.; Voevodin, A. A. Synthesis of Few-Layer, Large Area Hexagonal-Boron Nitride by Pulsed Laser Deposition. *Thin Solid Films* **2014**, 6–11.